PHYSICAL REVIEW FLUIDS **10**, 024001 (2025)

Editors' Suggestion

Experiments on buoyancy-driven instability ahead of a dissolution front in a porous rock

Sam Clarke,[1,*] Jon Harrington,[2] Simon Norris,[3] and Andy Woods[1]
[1]*Institute for Energy and Environmental Flows, University of Cambridge, Cambridge CB2 1TP, United Kingdom*
[2]*British Geological Survey, Keyworth, Nottingham NG12 5GG, United Kingdom*
[3]*Nuclear Waste Services Ltd, Calderbridge, Cumbria CA20 1DB, United Kingdom*

(Received 18 September 2024; accepted 19 December 2024; published 6 February 2025)

Fluid-rock reactions are of great interest in many engineered geological storage and disposal systems where the long term integrity of the system is key, and where fluid seepage through a permeable rock may lead to reaction and convective transport of material through the formation. If an unsaturated fluid displaces formation fluid in equilibrium with a reactive porous medium, a reaction front develops, across which the invading fluid becomes saturated with the soluble matrix material. Depending on the composition of the invading fluid, it may initially be less dense than the formation fluid, but following reaction it may become denser than the formation fluid. If the invading fluid displaces the formation fluid downwards through the porous layer, the reaction front may then be stabilized by buoyancy, but a Rayleigh-Taylor type instability can develop at the interface between the reacted fluid and the original formation fluid ahead of the reaction front. We present a series of new analog experiments of this process by injecting aqueous sugar solutions into a porous layer containing saturated salt solution, salt powder, and glass ballotini. As an analog of a reaction front, a dissolution front develops as the aqueous sugar solution dissolves the salt powder and becomes denser than the saturated salt solution. The buoyancy instability then leads to a growing finger interface. If the buoyancy speed of the fluid, u_B, is smaller than $u_F - u_R$, where the speed of the advancing fluid-fluid front is u_F and the speed of the dissolution front is u_R then the instability grows as if the system were unconfined. However, if $u_B > u_F - u_R$, then the supply of fluid at the dissolution front limits the growth of the instability. We present an idealised model for the speed of the non-linear buoyancy-driven fingers, and we consider the implications of our results for the long term integrity of a number of geological storage systems.

DOI: 10.1103/PhysRevFluids.10.024001

I. INTRODUCTION

In many situations in subsurface porous formations, fluid of one density and composition may invade and displace the original formation fluid which is in equilibrium with the host matrix. If the invading fluid is undersaturated with respect to a mineral in the matrix, a reaction front may develop [1,2]. The reaction can change the density of the injected fluid, leading to changes in the buoyancy

---

[*] Contact author: sc998@cam.ac.uk

relative to the original formation fluid. In turn, this may lead to buoyancy-driven instabilities which impact the speed at which the injected fluid migrates through the formation.

Such a situation may arise in several natural and industrial settings, including geothermal power systems [3,4], magmatic intrusions [5], and sinkholes in karstic landscapes [6,7]. In many geothermal power systems, cold water is injected into high temperature reservoirs to extract thermal energy. The formation water in the reservoir typically contains large quantities of dissolved gases such as CO_2 and SO_2. If the composition of the injected fluid is not controlled to match that of the reservoir fluid, reactions with the reservoir rock have the potential to generate significant secondary porosity in the rock [8] and density differences between the injected fluid and the formation fluid. In turn this can have implications for the sweep pattern of the injected fluid [9] and the effectiveness of the reinjection. A natural analog occurs when faulting connects different water masses in the subsurface [10], or when meteoric water infiltrates and dissolves a karstic subsurface following descent of the groundwater table, creating sinkholes [11]. In plutonic systems, crystals solidify from liquid magma and sink, forming a mush at the base of the chamber. New magma is periodically added from deeper reservoirs [12] and passes through the mush. The new magma is chemically distinct from the crystal mush, prompting chemical reactions, which can alter both the density of the new magma and the permeability of the mush [13].

In geological radioactive waste repositories, over geological time, fluid accumulated in a repository system, typically at one temperature and composition, may leak out into a surrounding reactive permeable rock through a fracture network where it may react, leading to changes in the buoyancy with respect to the formation pore water. Understanding such buoyancy-driven flows is critical for building a safety case for geological disposal of nuclear waste [14].

In the present paper we develop a series of idealized analog laboratory experiments to explore aspects of such reactions and the associated flow instabilities which result from the change in buoyancy of the fluid following reaction. To model a porous rock, we use a bead pack, also containing some solid salt powder. We initially fill the bead pack with saturated salt solution and we then displace this from above with an aqueous sugar solution, unsaturated in salt, and initially less dense than the saturated salt solution. As the fluid migrates downwards through the bead pack, the unsaturated injection fluid dissolves the salt powder producing a horizontal dissolution front which is stabilized by buoyancy. The injection fluid dissolves the salt powder across this front, and its density increases above that of the original saturated salt solution. This results in a potential buoyancy instability of the reacted injection fluid with respect to the formation fluid (Fig. 1). We explore the conditions under which this instability develops and its nonlinear evolution through our experiments. Although our experiments strictly relate to a dissolution front, the changes in the density and associated dynamics are analogous to several fluid-rock reactions [cf Phillips (1991)].

The paper is arranged as follows. First, we describe the experimental system. Next, we present a series of results from our experiments, illustrating the different instabilities observed. Finally, we develop an idealized model of the instability and compare this with the experimental measurements. We then discuss the relevance of these results for various applications.

II. EXPERIMENTAL SYSTEM

To simulate the displacement of fluid through a partially soluble permeable rock, we filled a 15 cm × 65 cm perspex cell of thickness 1 cm with a mixture of transparent glass ballotini of diameter 250 μm and NaCl crystals. The NaCl crystals were of approximately the same dimensions as the ballotini. The pack was set up by systematically adding small volumes of the salt-ballotini mixture to avoid separation of the glass and NaCl powder. The mass ratio of the ballotini and the salt powder in the cell was 87:13.

We then filled the cell with a saturated NaCl solution using a peristaltic pump connected to a central inlet on the bottom of the cell. The cell was continuously agitated during filling to prevent air bubbles becoming trapped. By measuring the volume of fluid added to the cell, and the depth of

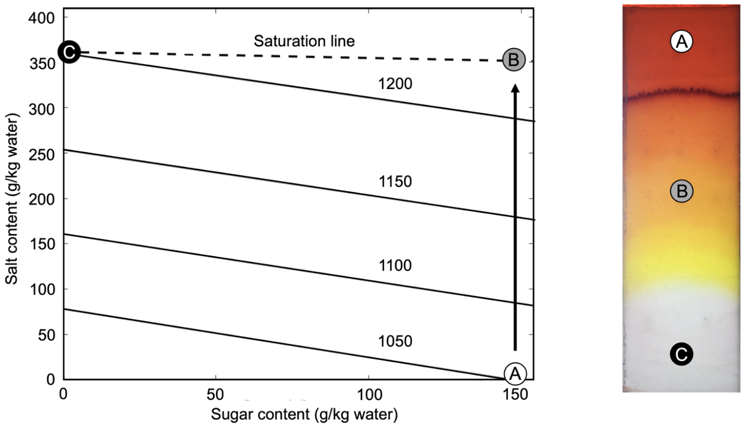

FIG. 1. Diagram showing contours of constant density as a function of salt concentration (y axis) and sugar concentration ($x$axis), in kg/m^3, following [15]. In the experiments, the original saturated salt solution in the pack is shown by the black circle, the sugar solution added to the top of the cell is shown by the white circle, and the sugar-salt solution is shown by the gray circle. The accompanying image from experiment 37, a typical experiment, illustrates the spatial location of the three fluid regions as the dissolution front and the fluid migrates downwards through the cell.

the pack, we estimated the porosity to be 33 ± 2% in each experiment. The cell was then filled with NaCl solution until its level was 3 cm above the top of the pack.

A sucrose solution was then prepared. By using varying concentrations of sucrose, we were able to manipulate the density and viscosity of the final salt-saturated fluid (Table I). The sucrose solution was dyed red using 2.5 g TRS red food coloring per liter of solution. A layer of depth 3 cm was slowly added above the saturated salt solution, using a siphon connected to a large reservoir. Owing to the density contrast, we did not observe any mixing with the saline solution.

The cell was placed in front of a MiniSun LightPad LED light sheet. During each experiment, pictures were taken every ten seconds using a NIKON 5900 camera positioned 145 cm from the center of the cell (see Fig. 2). Experiments involved the continued addition of the sucrose solution into the top of the tank. The rate of addition was fixed in each experiment, with values in the range 0.001–0.03 cc/s, using a peristaltic pump (Table II). The NaCl solution was extracted from the bottom of the tank at the same rate. The flow of the incoming fluid through the pack was inferred by following the interface between the original (clear) and the injected (red) fluids.

The dissolution of the salt results in a 16–19% increase in density of the injected fluid, and a near doubling of its viscosity (Table I).

TABLE I. Viscosity, μ (mPaS), and density, ρ (kg/m^3), of sugar and sugar-salt solutions.

	No salt		Salt-saturated	
Sugar content (g/l H_2O)	ρ	μ	ρ	μ
0	997	0.93	1198	1.74
50	1016	1.03	1209	1.98
100	1034	1.17	1219	2.35
150	1050	1.33	1230	2.73
200	1066	1.52	1240	3.42

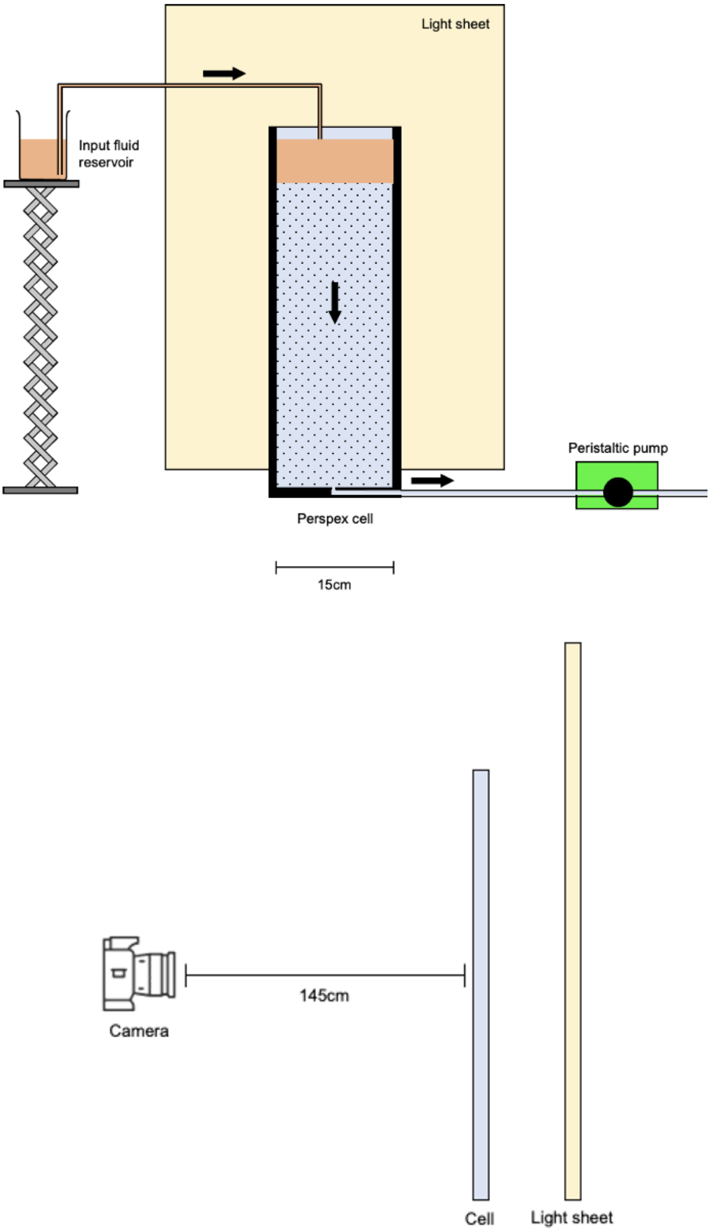

FIG. 2. Schematic of the experimental apparatus; front view (top) and side view (bottom).

III. EXPERIMENTAL OBSERVATIONS

In all experiments, as the sugar solution enters the porous pack, a localized horizontal interface becomes established. This may be seen in images of the experiment as a dark band which gradually migrates down through the pack. We refer to this as the dissolution front. We withdrew fluid samples from extraction ports above and below this band and measured their optical density with an Atago digital refractometer. Optical density is a good proxy for salinity, and so we can infer the salt content of each sample (see Fig. 3). These measurements show that the salinity of the injected water is zero in the upper part of the tank, but then gradually increases toward a maximum value, over a distance

TABLE II. Table of experiments.

Expt no.	Flow rate (10^{-3} cm^3/s)	Sugar content (g/l H_2O)	Density of salt-saturated injection fluid (g/cm^3)	u (10^{-6} m/s)	k (10^{-11} m^2)	u_B (10^{-6} m/s)
31	2.44	100	1.222	4.65	3.33	3.08
36	10.60	100	1.222	20.19	3.24	3.00
37	29.50	100	1.222	55.56	3.33	3.08
40	3.49	100	1.222	6.65	3.63	3.36
41	2.28	100	1.222	4.61	3.10	2.87
45	3.43	100	1.222	6.61	3.12	2.89
47	4.71	100	1.222	9.24	3.37	3.12
48	5.99	100	1.222	12.10	3.25	3.01
53	1.15	100	1.222	2.19	3.33	3.08
62	7.70	200	1.240	14.97	3.57	4.15
63	12.20	200	1.240	23.99	3.11	3.61
64	18.90	100	1.222	36.10	3.72	2.99
65	9.73	100	1.222	18.64	3.15	2.53
66	9.49	200	1.240	18.29	3.50	4.12
67	19.50	50	1.208	37.25	3.24	1.23
68	10.50	50	1.208	20.06	3.24	1.23
69	10.60	150	1.229	20.25	3.25	2.99
70	16.30	150	1.229	30.44	3.33	3.06
71	1.09	100	1.222	2.08	3.25	2.71
72	1.09	150	1.229	2.11	2.47	2.27

of 2 cm or so, and then remains constant. This corresponds to the solution becoming saturated in salt as it dissolves the salt powder in the cell. By comparison with our photographs, we see that the dark horizontal band corresponds to the point where the solution first becomes saturated in salt. This represents the end of the narrow dissolution zone. Analysis of the dye suggests that this dark band arises because the Allura red (E129) dye in the TRS red food coloring mixture is less soluble than salt. On injection to the cell, the Allura red is in solution, but as the mixture becomes saturated in salt, the Allura red precipitates from solution. This leads to the dark band at the dissolution front. As the dissolution front and the unsaturated injection fluid migrate down through the cell, the band of Allura red also migrates: this is because it redissolves in the unsaturated solution, migrates to the dissolution front, and then reprecipitates. The saturated injection fluid continues to move through the porous pack beyond the dissolution front (Fig. 1). The salt-saturated injection fluid emerging from the dissolution front is in fact denser than the original saturated aqueous salt solution owing to the presence of the sugar (Fig. 1). In the images, this salt-saturated injection fluid does still contain some dye: the food coloring also contains Tatrazine (E102), and this remains in the solution even when the solution is saturated in salt. The blue channel in the digital image of light intensity seen by the camera is sensitive to this dye, and hence enables us to identify the region where there is injected fluid and original formation fluid (see Fig. 4).

In Fig. 4 we present a series of five photographs taken at equal time intervals in three experiments carried out at different injection rates [(i) 37, (ii) 40, and (iii) 53, Table II]. Images are shown in visible color and, using false color, we also show the variation of the intensity of the blue channel. In experiment 37 (top), the injection speed is relatively high and the interface between the salt-saturated injection fluid and the original ambient fluid appears to be stable and nearly horizontal. In the unstable cases, the injection speed is smaller and the interface between the salt-saturated

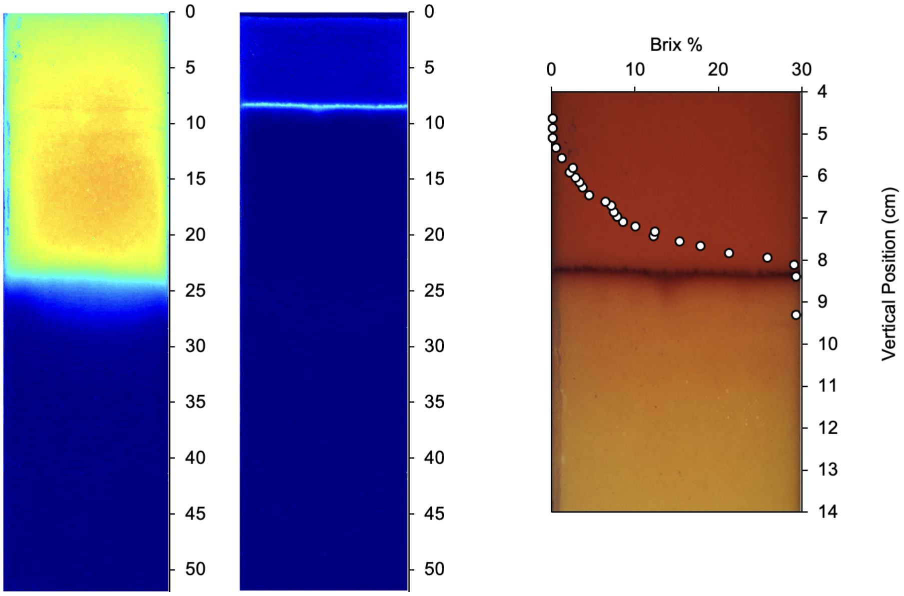

FIG. 3. False color images of the light intensity taken from the blue (left) and red (center) channel of the data of an image from a test experiment using fresh water as the input fluid. The blue channel is sensitive to the presence of Tatrazine in the food dye, and can be used to track the location of any input fluid. The red channel is sensitive only to Allura red which has precipitated, and therefore can be used to locate the dissolution front. Right: Brix data showing the variation of the salinity of the injected sugar solution as a function of height in the cell. The salt concentration increases to a maximum over a region about 2 cm deep, and then remains at this value in the sugar-salt solution further downstream in the cell. The point at which the solution becomes saturated in salt corresponds to the end of the reaction front; here the Allura red precipitates from solution as seen by the faint dark band in the central and right hand images.

injection fluid and the original formation fluid becomes irregular and unstable. In the unconfined case, (experiment 40, middle), the fluid-fluid instability grows relatively slowly compared to the injection speed. A uniform layer of salt-saturated injection fluid develops ahead of the dissolution front, and the unstable finger zone develops ahead of this region. With an even slower injection rate (experiment 53, bottom), the interface between the salt-saturated injection fluid and the original formation fluid is very unstable, and the nonlinear fingers which initially develop at the fluid-fluid front extend all the way back to the dissolution front. These experimental observations are now compared with a series of simplified models for the nonlinear buoyancy driven instability in the case that the fluid-fluid interface is unstable.

IV. MODEL FOR THE INSTABILITY

We propose that the instability of the fluid-fluid front arises owing to the larger density of the salt-saturated sugar solution which develops downstream of the dissolution front, above the original saturated salt solution. The Rayleigh-Taylor type buoyancy instability which tries to develop at the interface may be suppressed if there is a background flow and the displacing fluid is more viscous than the displaced fluid such that the change in the viscous pressure gradient exceeds the change in hydrostatic pressure gradient across the interface [1]. Linear stability analysis leads to the condition that a descending fluid-fluid front is stable if

$$\frac{\mu_1 - \mu_2}{k} u\phi > g(\rho_1 - \rho_2), \tag{1}$$

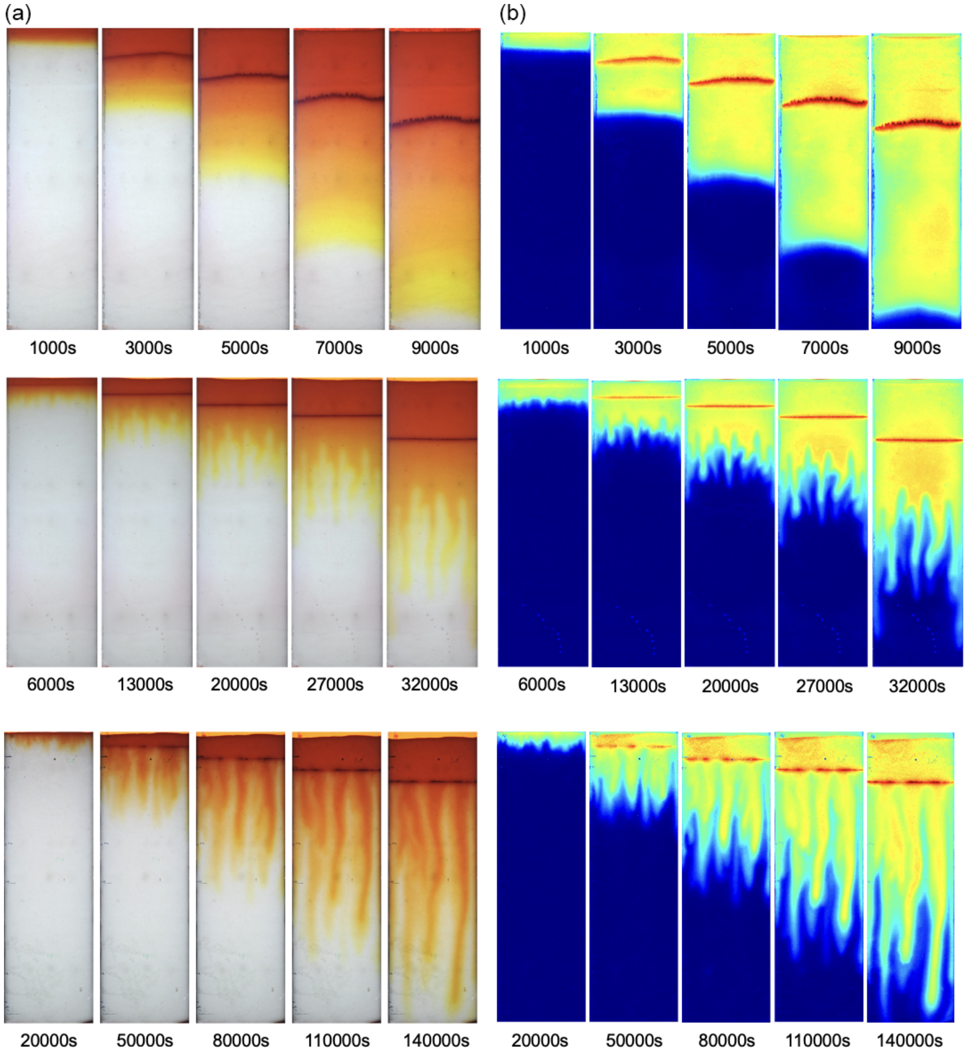

FIG. 4. A series of five images, taken at equal time intervals, during each of three experiments; expt 37 (top), 40 (middle), and 53 (bottom)—see Table II. The images in panel (a) show the original photographs, and in panel (b) show false color images of the intensity of the blue channel from the digital photographs. Experiment 37 shows a stable fluid-fluid interface; experiment 40 shows an unstable fluid-fluid interface in which the fingers remain ahead of the dissolution front, and experiment 53 shows an unstable fluid-fluid interface in which the fingers reach the dissolution front.

where μ_1 and ρ_1, and μ_2 and ρ_2 are the viscosity and density of the displacing and displaced fluids, respectively, k is the permeability, ϕ is the porosity, u is the Darcy speed of the background uniform flow, and g is the gravitational acceleration.

In Fig. 5 we compare the conditions as measured in a subset of our experiments (Table II) with the stability condition above as shown by the solid line. To estimate the permeability of the salt-bead system, k, in the experiments, as required to estimate the viscous pressure gradient, we carried out a draining experiment in which we measured the rate at which a saturated aqueous salt solution supplied at the top of the tank descended under gravity through the salt-ballotini pack.

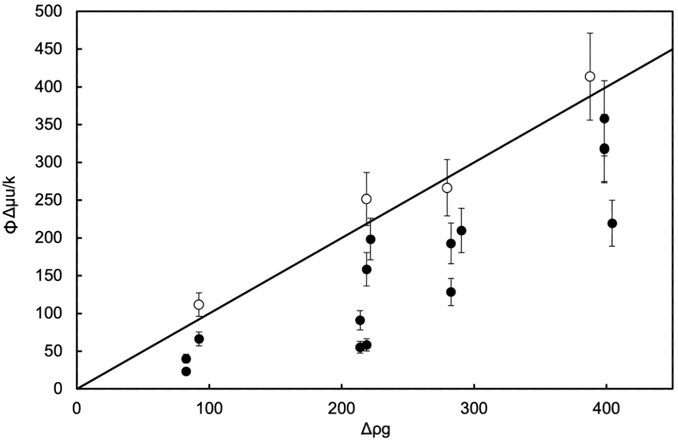

FIG. 5. Comparison of our observations from the laboratory experiments and the theoretical condition for instability, based on linear instability theory. Experiments observed in which the fluid-fluid front is stable are shown with open circles, while those observed to be unstable are shown by solid circles.

Experiments in which the fluid-fluid interface was observed to remain stable are shown by open symbols and those in which the interface is unstable are shown by solid circles. It is seen that the experiments are consistent with the linear stability condition (Eq. (1) from [1]).

A. Observations of the nonlinear finger growth

We now explore the nonlinear development of the fingers. We estimate the upper and lower boundary of the finger region at the fluid-fluid front as follows. We first subtract an image of the tank without any dyed fluid, taken at the start of the experiment from all subsequent frames. These resulting digital images include data for the red, green, and blue color channels: the blue channel is sensitive to the Tatrazine in the food coloring, and so we use this channel to identify where the (reacted) input fluid is in the pack. We average the value of the blue channel along each horizontal row of pixels, and plot this as a function of vertical position along the pack (Fig. 6). We see that, in the region of the nonlinear fingers, the average value of the blue channel decreases approximately linearly with vertical distance, while higher in the cell, the data has a nearly constant value corresponding to the supply fluid, and below the finger zone, the data fall to zero. We then use the best straight-line fit to this data to identify (i) the upper boundary of the finger zone, X_T, as the highest point where the data intersects the fitted line, and (ii) the lower boundary, X_L, as the point where the value of the blue channel on the fitted line reaches zero.

Using a series of images equivalent to Fig. 6 taken at regular time intervals during each experiment, we calculate the location of the leading and trailing edge of the finger zone as a function of time. We have done this for all experiments listed in Table II. In Fig. 9 we summarize our measurements, illustrating how u_L/u and u_T/u, the speeds of the fluid in the "descending" and "ascending" fingers, $\frac{dX_L}{dt}$ and $\frac{dX_T}{dt}$, scaled by the Darcy speed of the fluid, u, vary as a function of the ratio of the buoyancy speed, u_B, to u. Here u_B is given by

$$u_B = \frac{k\Delta\rho g}{\mu_1}, \tag{2}$$

where μ_1 is the viscosity of the salt-saturated sugar solution, and $\Delta\rho$ is the difference in density between the salt-saturated sugar solution and the salt-saturated aqueous solution. In the figure we also show the speed of the dissolution front, u_R as a fraction of u.

It is seen that at a critical value of u_B/u, the speed of the trailing edge of the fingers u_T matches the speed of the dissolution front, u_R. For smaller values of u_B the fingers are unconfined in the

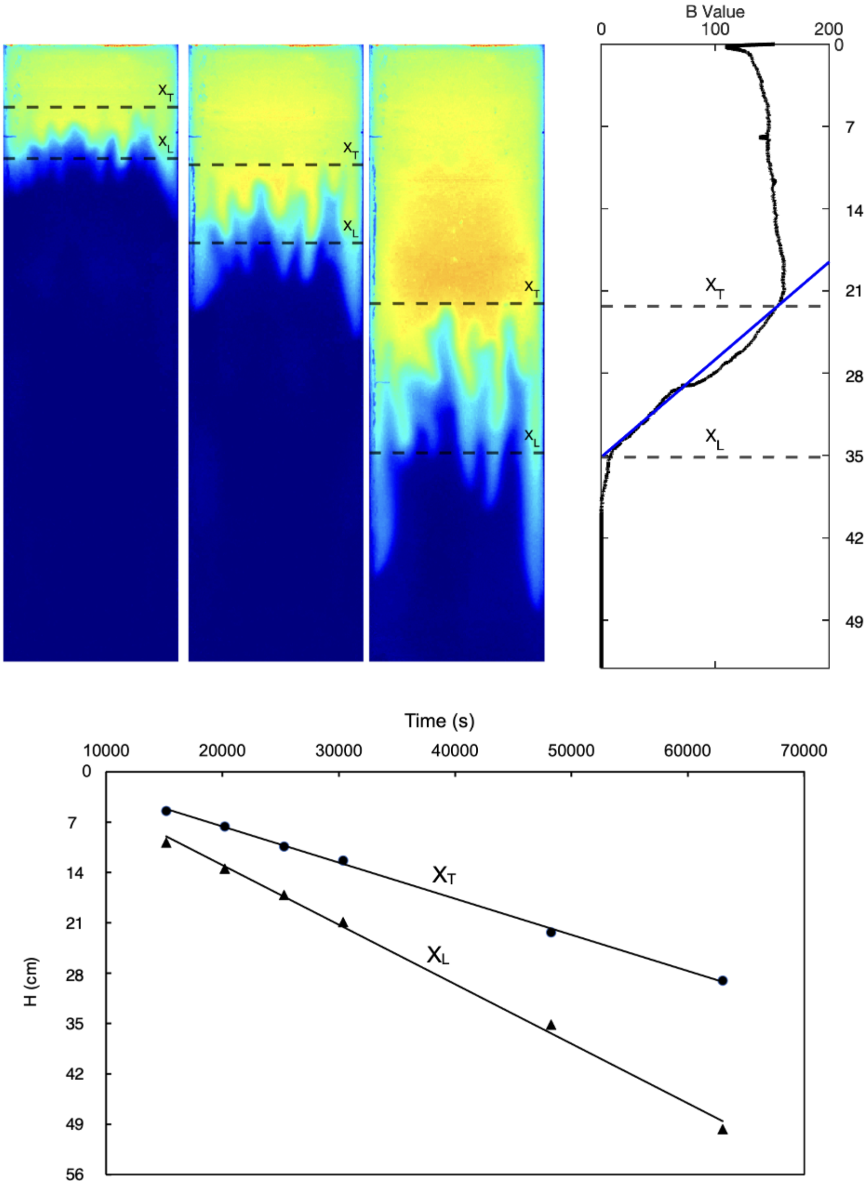

FIG. 6. Top row: Image from experiment 45 to illustrate the nonlinear fingers. The figure is generated from the blue channel of the original RGB digital image. Top right: horizontal average of the blue channel as a function of vertical position in the right hand image. Blue line is the linear fit used to identify the upper and lower extent of the finger zone, X_T and X_L. Bottom: variation of the finger zone boundaries as a function of time for this experiment.

sense that $u_T > u_R$, whereas for larger values of u_B the speed of the trailing edge of the fingers is constrained by the speed of the dissolution front, $u_T = u_R$.

In describing the finger zone, it is also of interest to explore the fraction of the cell filled with dense fingers and the fraction containing original formation fluid. To this end, we have plotted the horizontal line of pixels located at the theoretical planar fluid-fluid interface (in the absence of fingers) as a function of time (Fig. 7) for a series of experiments. In each figure, time increases

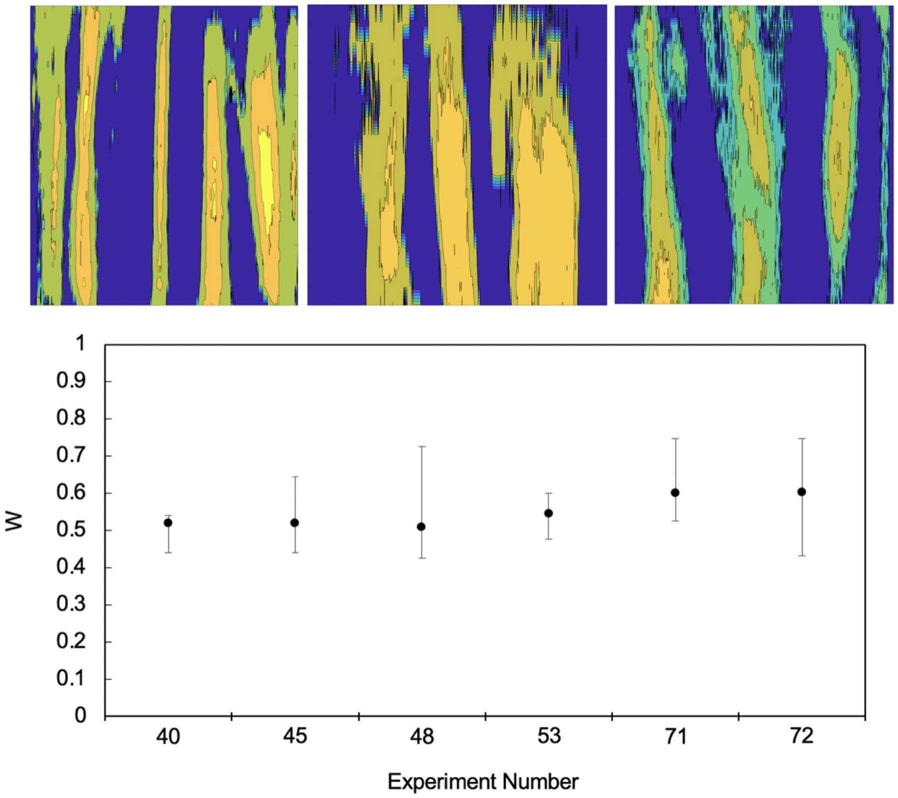

FIG. 7. Top row: Variation over time of the light intensity, at the theoretical planar fluid-fluid location, in the intermingled finger zone for experiments 40 (left column), 53 (centre column), and 71 (right column). The images illustrate that over time the fingers are quite stable, appearing not to merge or pinch out. Bottom: Average width of the center of the finger zone for several experiments measured at the midpoint of the finger zone (circles). Error bars show the maximum and minimum widths over the course of each experiment.

downwards along the vertical axis. It is seen that the width of the fingers is approximately constant over time, with the individual fingers retaining their identity, and there is little evidence of finger merging over the duration of our experiment. At each time we have estimated the fraction of the total width of the tank occupied by the fingers by thresholding the light attenuation signal through the tank to distinguish dyed and undyed fluid. This suggests that in all experiments the fractional width of the cell occupied by the descending fingers, at the level of the theoretical planar fluid-fluid front was in the range 0.45–0.55 (Fig. 7).

We now develop some idealized models for the speed of the dissolution front, based on the assumption of equilibrium dissolution, and for the growth rate of the nonlinear fingers, based on the buoyancy difference between the saturated sugar-salt solution, and the original saturated salt solution, to provide a reference to help interpret the data shown in Fig. 9.

V. THE DISSOLUTION FRONT

The location of the idealized dissolution front can be calculated in terms of a mass balance. We suppose that the dissolution front has speed λu, where u is the Darcy speed of the flow ahead of the dissolution front. If ϕ is the original pack porosity, then the fluid-fluid front moves with speed $u\phi$. If the salt powder represents a volume fraction S of the solid matrix, then at time t the mass of salt dissolved from the original matrix in the region upstream of the dissolution front, $\rho_s S(1-\phi)\lambda u t$, has been transferred to the saturated injection fluid downstream of the dissolution front, which has concentration C_s and hence salt mass $\rho_{ss} C_s u(1-\phi\lambda)t$, where ρ_s is the salt density and ρ_{ss} is the density of the saturated sugar-salt solution. Equating these expressions we find that

$$\lambda = \frac{\rho_{ss} C_S}{\phi \rho_{ss} C_S + \rho_s S(1-\phi)}. \tag{3}$$

In Fig. 9, the measured speed of the dissolution front is compared to the interstitial speed. For our experiments, we expect λ to have a value of order 0.33 with an error of order 10% associated with spatial variations in porosity and salt content of the pack, as well as heterogeneities in salt distribution which can occur during filling.

VI. FINGER DYNAMICS

We now develop an idealized model for the nonlinear development of the finger zone. The observations above suggest that the fingers are relatively long and thin and that at a given fractional distance between the trailing and leading edge of the finger zone, the fingers originating from the salt-saturated sugar solution occupy a constant fraction of the width of the cell. Although in the laboratory frame, all the fluid moves downwards, in the frame of reference of the theoretical planar fluid-fluid front, the sugar-salt fingers move downwards and the salt fingers move upwards.

The typical speed of the fingers in the experiments is 10^{-5} m/s, while the width of the fingers is about 1.0 cm. The molecular solutal diffusion coefficient is about $D \sim 10^{-9}$ m^2/s, and the fingers have buoyancy speed of order 10^{-5} m/s. With beads of size 10^{-4} m, these values suggest that the transverse dispersion coefficient in the cell, which we expect to scale as ud, is smaller than 10^{-9} m^2/s (cf [1,2]). As a result, any transverse mixing across the fingers will extend a distance of order $l \sim (DL/u)^{1/2}$ over a finger zone of vertical extent L. With fingers of length $0.1 - 0.2$ m, this suggests a transverse mixing length of order 10^{-3} m which is much smaller than the finger width, so to leading order we neglect dispersive mixing between the upflow and downflow fingers in developing a simplified model for the dynamics. We consider the unconstrained and then the constrained fingering regimes.

A. Unconstrained finger zone

We assume the fingers are long and narrow, so the pressure in the finger zone is approximately uniform in the horizontal direction, with the buoyancy difference between the two fluids driving the up and down flow relative to the mean down flow. Neglecting the effects of any transverse diffusion in the finger zone, we assume the Darcy speed in the finger zone is $\overline{u} + u_i$, where $\overline{u}$ is the background Darcy speed, z is the vertical coordinate along the cell, and u_i denotes the speed of upflowing fingers ($i = 2$) and the downflowing fingers ($i = 1$) relative to the mean downflow (Fig. 8). The buoyancy associated with the salt-saturated sugar solution, with sugar concentration c_1, relative to the salt-saturated aqueous fluid, with no sugar, is $g'(c_1) = g\beta c_1$, where β is the sugar expansion coefficient. Darcy's law then implies

$$\overline{u} + u_i = -\frac{k}{\mu_i}\left[\frac{dp}{dz} - \rho_o g'(c_i)\right], \tag{4}$$

where $c_2 = 0$ and ρ_o is a reference density.

From the overall mass balance,

$$u_1 w + u_2(1-w) = 0 \tag{5}$$

in the finger zone, where $w(z)$ is the width of the descending fingers as a fraction of the width of the cell. This leads to the expression for the flow speed u_1 in terms of the buoyancy and

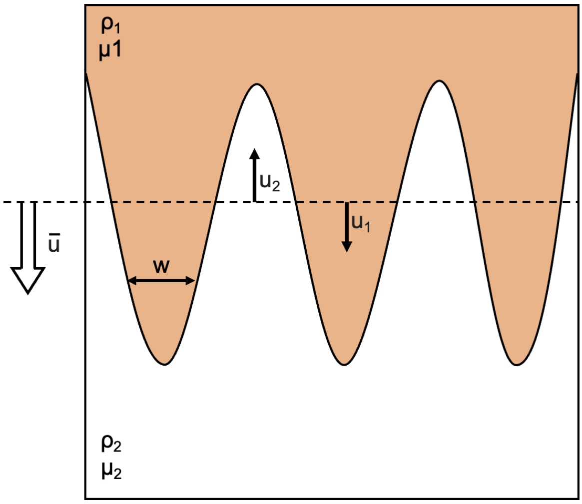

FIG. 8. Schematic of the buoyancy instability, showing how velocity perturbation u_i from interstitial velocity $\bar{u}$ causes the fingers to grow. Color represents fluid composition: orange is salt-saturated sugar solution, clear is salt-saturated aqeuous solution.

the finger width

$$u_1 = \left[\bar{u}\left(1 - \frac{\mu_1}{\mu_2}\right) + \frac{k\rho_o g'}{\mu_2}\right]\left[\frac{(1-w)}{w + (1-w)\frac{\mu_1}{\mu_2}}\right]. \tag{6}$$

In the frame moving downwards with the mean flow, the width of the descending finger zone can change owing to vertical variations in w, as given by the mass balance

$$\phi\frac{\partial w}{\partial t} + \frac{\partial(u_1 w)}{\partial z} = 0. \tag{7}$$

This implies that surfaces of constant w advect with characteristic speed

$$\frac{dz}{dt} = \frac{1}{\phi}\left[\bar{u}\left(1 - \frac{\mu_1}{\mu_2}\right) + \frac{k\rho_o g'}{\mu_2}\right]\left(\frac{-w^2 + \frac{\mu_1}{\mu_2}(1-w)^2}{\left[w + \frac{\mu_1}{\mu_2}(1-w)\right]^2}\right). \tag{8}$$

Relative to the moving frame, this model suggests that the top of the finger zone, where $w = 1$, has upward speed

$$\frac{dz}{dt} = \frac{1}{\phi}\left[\bar{u}\left(1 - \frac{\mu_1}{\mu_2}\right) + \frac{k\rho_o g'}{\mu_2}\right] \tag{9}$$

and the leading front of the finger zone, where $w = 0$, has downward speed

$$\frac{dz}{dt} = \frac{1}{\phi}\left[\bar{u}\left(\frac{\mu_2}{\mu_1} - 1\right) + \frac{k\rho_o g'}{\mu_1}\right]. \tag{10}$$

Also, when

$$w = \frac{V^{1/2}}{1 + V^{1/2}}, \tag{11}$$

where the viscosity ratio $V = \mu_1/\mu_2$, the speed of the finger zone is zero relative to the background flow. In the present experiments, $V \approx 1.3$, suggesting that the width of the finger zone at the theoretical fluid-fluid front is $w \approx 0.53$ consistent with the measurements in Fig. 7.

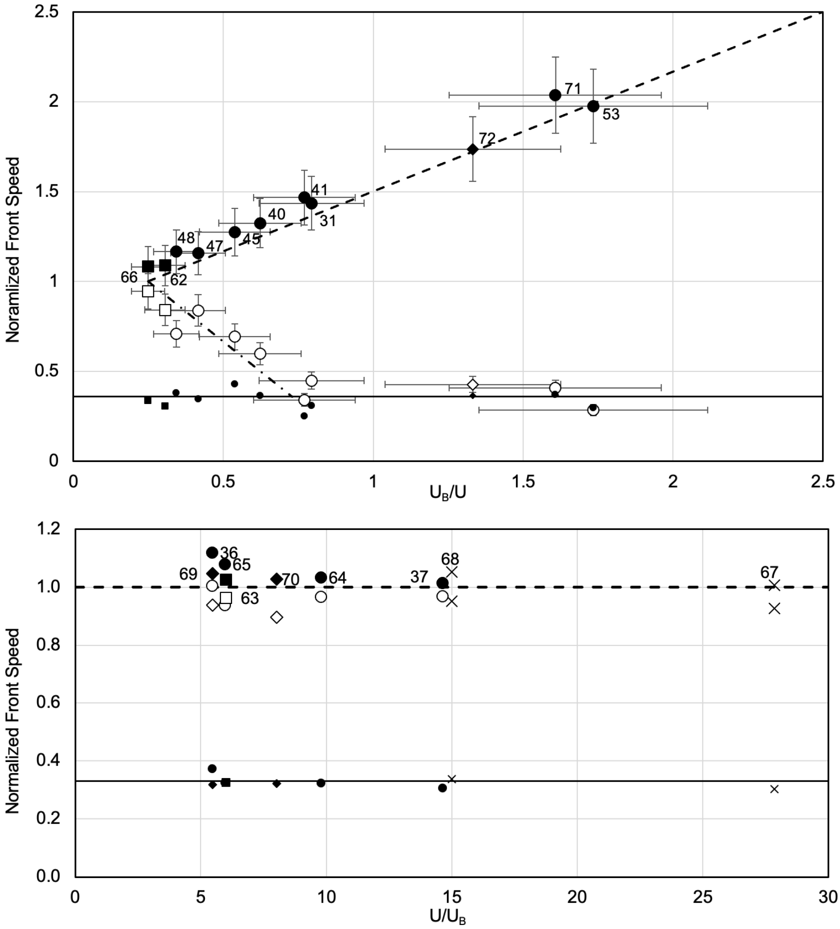

FIG. 9. Speed of the leading (filled) and trailing (blank) edge of the finger zone, and the speed of the dissolution front (small symbols), all normalized by the injection speed, as a function of the ratio of the buoyancy speed to the injection speed. The dashed lines show the speed of the leading and trailing edges of the finger zone for the 100g/l experiments, and the solid line shows the speed of the dissolution front according to the model. Symbols indicate the sugar content of the injection fluid in g per liter water: 50 (crosses), 100 (circles), 150 (diamonds), and 200 (squares). Top graph shows cases unstable to buoyancy, bottom graph shows cases stable to viscosity.

We compare the above simplified prediction of the location of the leading and trailing edge of the finger zone with the experimental observations in Fig. 9. There is reasonable agreement over the range of experiments reported in Table II in which the speed of the upstream end of the finger zone is greater than the speed of the dissolution front. As the interface is stretched out by the fingers, the average sugar gradient across this zone decreases inversely with the length of the fingers, in accord with the data of Fig. 5. Eventually the effects of transverse dispersive mixing across the fingers may become significant, but the scalings above suggest this occurs a later time than in the present experiments.

As a further comparison, in Fig. 10, the green line shows the model prediction for the width of the descending fingers, as a fraction of the total width of the experimental cell, w, as a function of the vertical position in the finger zone. This has been calculated using the advection speed of surfaces of constant w, and scaled with the distance traveled by the leading edge of the descending fingers where $w = 0$, relative to the theoretical planar fluid-fluid front position. The figure also

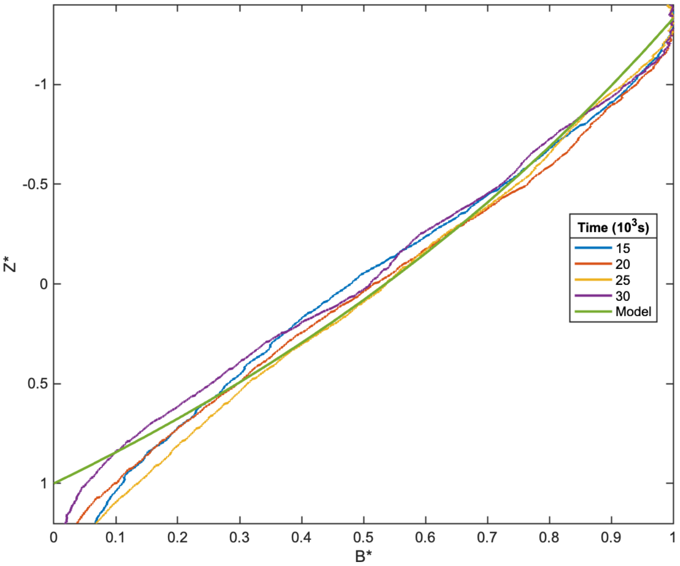

FIG. 10. Variation of the width of the descending fingers in the finger zone as a function of position across the finger zone as predicted from the model (green line). The vertical position, Z*, has been normalized so that the location of the theoretical fluid-fluid front is zero and the position of the trailing edge of the fingers is -1.33. The figure also shows the horizontal average of the blue channel, B*, calculated from four digital images, taken at different times, during experiment 45. The horizontal average has been normalized to have value one at the top of the finger zone, and value zero at the base of this zone, and hence provides a proxy for the fraction of the cell containing descending fingers as a function of depth.

shows the horizontal average of the intensity of the blue channel in images recorded at four times during experiment 45. This has been normalized with the intensity just above the finger zone, and represents an approximate measure of the net finger width as a function of position in the finger zone. These data are in reasonable accord with the model.

B. Constrained finger zone

In the case that the dissolution front speed exceeds the speed of the trailing edge of the finger zone as predicted above, then the trailing edge of the finger zone terminates at the dissolution front, moving with speed λu, since the aqueous sugar solution which is supplied upstream of the dissolution front is less dense than the saturated salt solution originally in the formation ahead of the dissolution front.

Meanwhile, the leading edge of the saturated sugar-salt solution extends ahead of the theoretical planar fluid-fluid front as before. Comparison of this picture of the finger development is consistent with the data shown in Fig. 9.

VII. DISCUSSION AND CONCLUSION

In this paper, we have presented a series of experiments in which an unsaturated fluid invades a partially soluble porous matrix from above, such that the injected fluid is less dense than the original formation fluid. This leads to a stable, horizontal dissolution front which gradually descends through the tank. The fluid emerging from the dissolution front becomes saturated in salt, increasing the density of this fluid relative to the original formation fluid leading to a Rayleigh-Taylor instability at the fluid-fluid front.

Our data are consistent with the classical linear instability model for the onset of instability. In the case of relatively fast flow, the finger zone is all located ahead of the moving dissolution front.

However, when the fluid is supplied more slowly, the trailing edge of the fingers meet the dissolution front and this leads to a constrained supply of fluid to the finger zone. A simplified nonlinear model for the evolution of the finger zone, based on a nonlinear kinematic wave model and neglecting the effects of dispersion, predicts a finger zone which is approximately of the same vertical extent as the experimental observations for the experiments.

By analogy, the instability of this dissolution front in our experiments is of considerable interest in permeable rocks where one fluid is injected into a reactive porous layer initially filled with a second fluid such that the injected fluid may be stable relative to the original formation fluid, but on reaction with the porous layer, the interface between the original and injected fluid becomes unstable. Once the interface is unstable, the injected fluid can mix a significant distance into the formation, and may not flood the formation as a conformal flow front, but in a finger regime, only partially saturating the formation. This may lead to injected fluid migrating further into a formation, and hybrid zones of fluid developing ahead of the reaction front. Much fascinating work has been carried out exploring infiltration instabilities: the present analysis is complementary to these studies and identifies that there may be instabilities of the fluid-fluid system even if the reaction is stabilized by gravity.

The processes may be relevant in interpreting some tracer data in geothermal systems, where cold fluid is injected to recharge the system. If this cold fluid is compositionally less dense than the formation fluid, but initially so cold that is it denser than the formation fluid, then it may initially spread over the lower part of the formation, but as it heats up it will become buoyant relative to the formation fluid. It may then finger through the original formation fluid to the top of the system. This may lead to early arrival of tracers at observation wells relative to the advective speed associated with the injection. As an idealized example, if the thermal density contrast is of order 0.01%, this can stabilize a compositional contrast of comparable magnitude. The associated buoyancy speed in a formation of permeability $10^{-12} - 10^{-13}$ m^2 would be of order $10^{-7} - 10^{-8}$ m/s. If water is injected along a line well, for example of length 1000 m, with a flow rate of 0.001–0.0001 m^3/s, and the the supply flow spreads over a zone 10–100 m from the well, then the supply speed, per unit area, would be of order $10^{-8} - 10^{-9}$ m/s. As a result, once the fluid passes the thermal front, it could become unstable and rise as fingers through the formation. This may lead to anomalously early breakthrough of the injected fluid to points much higher in the formation.

In geological waste repositories designed for disposal of nuclear waste, water may be generated over long time scales and this may eventually leak out into the formation. If the host rock contains minerals which are soluble in this water, this may lead to density changes of the fluid which then impacts the dispersal of the reacted fluid. This may be key for predicting the spatial distribution with time of any radionuclides which may migrate with the reactive fluids as they slowly leak from the geological disposal facility. This is particularly relevant to repositories built in halite rock (e.g., [16]).

In closing, we note that the instability described in this paper has been described as a two dimensional process, and it would be interesting to explore the analogous system in a three dimensional experimental tank. Also, the instability we have described relates to the advection of the dissolution front and the change in density associated with this. There are other instabilities which can arise when there is no net motion, and these are associated with the differential diffusion of salt and sugar across the interface which then can lead to a change in density as a double-diffusive instability [17,18], or a result of the different advection speed of a dissolving and nondissolving species, which can lead to a reversal of buoyancy if there is a perturbation of the interface, as in the double-advective instability described by Phillips (1991). However, in the present problem, the net migration of the fluid interface and the slower migration of the dissolution front, leads to generation of the unstable intermediate zone of fluid between the original formation fluid and the original supply fluid. We plan to explore whether the present experimental system can shed new insights into these other modes of instability.

ACKNOWLEDGMENTS

This work was supported by the Engineering and Physical Sciences Research Council (Grant No. 2395290).

[1] O. M. Phillips, *Flow and Reactions in Permeable Rocks* (Cambridge University Press, Cambridge, UK, 1991).

[2] A. W. Woods, Geothermal power and heat storage, in *Flow in Porous Rocks: Energy and Environmental Applications* (Cambridge University Press, Cambridge, UK, 2014), pp. 227–261.

[3] N. Yanagisawa, I. Matsunaga, H. Sugita, M. Sato, and T. Okabe, Temperature-dependent scale precipitation in the hijiori hot dry rock system, japan, Geothermics **37**, 1 (2008).

[4] E. Gunnlaugsson, H. Ármannsson, S. Thorhallsson, and B. Steingrímsson, Problems in geothermal operation - scaling and corrosion, in *Short Course VI on Utilization of Low- and Medium-Enthalpy Geothermal Resources and Financial Aspects of Utilization* (United Nations University Geothermal Training Programme, 2014), https://geocom.geonardo.com/assets/elearning/3.3.UNU-GTP-SC-18-19.pdf.

[5] W. Kruger and R. Latypov, Magmatic karst reveals dynamics of crystallization and differentiation in basaltic magma chambers, Sci. Rep. **11**, 7341 (2021).

[6] F. Gutiérrez, A. Cooper, and K. Johnson, Identification, prediction, and mitigation of sinkhole hazards in evaporite karst areas, Envrionmental Geology **53**, 1007 (2008).

[7] E. Shalev, V. Lyakhovsky, and Y. Yechieli, Salt dissolution and sinkhole formation along the dead sea shore, J. Geophys. Res.: Solid Earth **111**, B3 (2006).

[8] Y. Liu, S. Jin, Q. Cao, and W. Zhou, Tertiary hydrothermal activity and its effect on reservoir properties in the xihu depression, east china sea, Petroleum Science **16**, 14 (2019).

[9] T. Menand, A. Raw, and A. W. Woods, Thermal inertia and reversing buoyancy in flow in porous media, Geophys. Res. Lett. **30**, 2002GL016294 (2003).

[10] S. E. Ingebritsen, S. Geiger, S. Hurwitz, and T. Driesner, Numerical simulation of magmatic hydrothermal systems, Rev. Geophys. **48**, RG1002 (2010).

[11] J. G. Newton, *Development of Sinkholes Resulting from Man's Activities in the Eastern United States*, Circular 968 (U.S. Geological Survey, 1987), https://pubs.usgs.gov/circ/1987/0968/report.pdf.

[12] G. M. Brown, The layered ultrabasic rocks of rhum, inner hebrides, Philos. Trans. R. Soc. London, Ser. B **240**, 1 (1956).

[13] R. Didonna, F. Costa, H. Handley, S. Turner, and J. Barclay, Dynamics and timescales of mafc–silicic magma interactions at soufrière hills volcano, montserrat, Contrib. Mineral. Petrol. **177**, 28 (2022).

[14] Radioactive Waste Management Ltd, Geological disposal generic environmental safety case, Disposal System Safety Case Report DSSC/203/01 (Nuclear Decommissioning Authority, 2016), https://assets.publishing.service.gov.uk/media/5a82361e40f0b6230269b6f2/NDA_Report_no_DSSC-203-01_-_Geological_Disposal_-_Generic_Environmental_Safety_Case_-_Main_Report.pdf.

[15] P. Bohuon, M. Le Maguer, and A. L. Raoult-Wack, Densities and viscosities of ternary systems of nacl-sucrose-water, J. Chem. Eng. Data **42**, 266 (1997).

[16] R. M. Holt and D. W. Powers, valuation of halite dissolution at a radioactive waste disposal site, andrews county, texas, Geol. Soc. Am. Bull. **122**, 1989 (2010).

[17] S. E. Pringle and R. J. Glass, Double-diffusive finger convection: Influence of concentration at fixed buoyancy ratio, J. Fluid Mech. **462**, 161 (2002).

[18] C. Cooper, R. J. Glass, and S. W. Tyler, Experimental investigation of the stability boundary for double-diffusive finger convection in a hele-shaw cell, Water Resour. Res. **33**, 517 (1997).